Revision 2

Word Count: 6255

Composition-dependent thermal equation of state of B2 Fe-Si alloys at high pressure

Shunpei Yokoo[1], Eric Edmund[2,*], Guillaume Morard[2,3], Marzena Anna Baron[2], Silvia Boccato[2], Frédéric Decremps[2], Kei Hirose[1,4], Anna Pakhomova[5], Daniele Antonangeli[2]

1 - Department of Earth and Planetary Science, The University of Tokyo, Tokyo 113-0033, Japan.

2 - Sorbonne Université, Muséum National d'Histoire Naturelle, UMR CNRS 7590, Institut de Minéralogie, de Physique des Matériaux et de Cosmochimie, IMPMC, 75005 Paris, France.

3 - Université Grenoble Alpes, Université Savoie Mont Blanc, CNRS, IRD, Univ. Gustave Eiffel, ISTerre, 38000 Grenoble, France.

4 - Earth-Life Science Institute, Tokyo Institute of Technology, Meguro, Tokyo 152-8550, Japan.

5 - Photon Science, Deutsches Elektronen-Synchrotron, D-22607 Hamburg, Germany.

* - Current address: Earth & Planets Laboratory, Carnegie Institution for Science, Washington, DC 20015, USA.

ABSTRACT

Solid iron-silicon alloys play an important role in planetary cores, especially for planets that formed under reducing conditions, such as Mercury. The CsCl (B2) structure occupies a considerable portion of the Fe-Si binary phase diagram at pressure and temperature conditions relevant for the core of Mercury, yet its thermodynamic and thermoelastic properties are poorly known. Here, we report in situ X-ray diffraction measurements on iron-silicon alloys with 7–30 wt% Si performed in laser-heated diamond anvil cells up to ~120 GPa and ~3000 K. Unit-cell volumes of the B2 phase at high pressures and high temperatures have been used to obtain a composition-dependent thermal equation of state of this phase. In turn, the thermal equation of state is exploited to determine the composition of the B2 phase in hcp+B2 mixtures at 30–100 GPa and to place constraints on the hcp+B2/B2 phase boundary, determined to vary between ~13–18 wt% Si in the considered pressure and temperature range. The hcp+B2/B2 boundary of Fe-Si alloys is observed to be dependent on pressure but weakly dependent on temperature. Our results, coupled with literature data on liquid equations of state, yield an estimation of the density contrast between B2 solid and liquid under Mercury's core conditions, which directly relates to the buoyancy of the crystallizing material. While the density contrast may be large enough to form a solid inner core by gravitational sinking of B2 alloys in an Si-rich core, the density of the B2 solid is close to that of the liquid at solidus conditions for Si concentration approaching ~10 wt% Si.

Keywords: Fe-FeSi system, equation of state, phase diagram, high pressure experiment, planetary interiors, Mercury, inner core

INTRODUCTION

The abundance of metallic iron and silicate minerals in telluric planets leads to the expectation that iron-silicon alloys play a large role in planetary cores when formed under reducing conditions (Kilburn and Wood 1997; Ricolleau et al. 2011). Varying quantities of silicon alloyed with iron have been invoked to explain seismological observations of Earth's core (e.g. Fischer et al. 2012; Badro et al. 2015; Antonangeli et al. 2018) and geodetic observations of Mercury (e.g. Knibbe and van Westrenen 2018; Genova et al. 2019; Terasaki et al. 2019). In order to accurately model the interior structure and dynamics of these planets, the phase diagram of Fe-Si alloys at high pressure (*P*) and high temperature (*T*) and the thermal equations of state (EoS) of stable phases are crucial. In particular, the high S/Si ratio and low FeO content of Mercury's surface indicate that its interior is likely to be highly reduced (Nittler et al. 2011), leading to expected bulk core Si concentrations in excess of 12 wt% Si (Chabot et al. 2014; Knibbe and van Westrenen 2018; Terasaki et al. 2019). Consequently, the chemical and elastic properties of Si-rich Fe-Si alloys are key to understanding the present state and dynamics of Mercury's core.

Iron-silicon alloys at ambient pressure exhibit a complex phase diagram, with a series of solid solutions over a wide compositional range, in addition to several stoichiometric compounds such as FeSi, Fe_5Si_3, and Fe_2Si (Cui & Jung 2017). Stoichiometric FeSi has a B20 structure at ambient conditions (FeSi is the B20 structure prototype) and transforms into a B2 (CsCl type) structure at pressures above 30–40 GPa at high *T* (Fischer et al. 2013; Geballe & Jeanloz 2014). On the other side, at these pressures, the pure Fe end member exhibits fcc structure at high *T* and hcp structure at lower *T*, and its stability field expands by the addition of silicon (Brosh et al. 2009; Komabayashi et al. 2009; Komabayashi et al. 2019). Other stoichiometric compounds in the Si-rich side of the Fe-Si system such as Fe_2Si and Fe_5Si_3 are reported to be unstable with increasing *P* and *T* (Ponomareva et al. 2009; McGuire et al. 2017) although exact phase boundaries are poorly constrained. The coexistence field of B2 and hcp phases is also poorly constrained at high *P*-*T* (Kuwayama et al. 2009; Fischer et al. 2013). Specifically, the boundary between the hcp and hcp+B2 regions has been constrained experimentally by observing the decomposition of the hcp phase to an hcp+B2 mixture with increasing *T* (Kuwayama et al. 2009; Lin et al. 2009; Fischer et al. 2013; Tateno et al. 2015). In contrast, only a few experimental results were obtained for the transition from an hcp+B2 mixture to a single B2 phase (Fischer et al. 2013). Kuwayama et al. (2009) addressed the compositions of coexisting hcp and B2 phases at 45 GPa, but electron microprobe measurements performed on samples with small grains are extremely challenging, as the analysis of each individual grain is affected by spurious signals from the surrounding grains, which leads to an underestimation of the compositional difference between the two phases.

Densities of the Si-rich Fe-Si alloys are also not well known. Room-*T* and high-*T* equations of state of stoichiometric B2 FeSi have been addressed by several high-*P* studies (Sata et al. 2010; Ono 2013; Fischer et al. 2014). Conversely, with few exceptions (Edmund et al. 2019b), thermoelastic properties of non-stoichiometric B2/DO_3 alloys are largely limited to compositions which are commercially available, i.e. 8–9 wt% Si or 16–18 wt% Si (Lin et al. 2003; Hirao et al. 2004; Fischer et al. 2012; Fischer et al. 2014).

While for the Si-poor hcp structure the thermal equation of state varies only marginally with Si content compared to pure iron (Edmund et al. 2019a; Fei et al. 2016; Tateno et al. 2015), studies on the Si-rich B2 structure indicate that elastic and thermal parameters strongly depend on Si content (Fischer et al. 2012, 2014; Edmund et al. 2019b). Since the B2 stability field is expanded significantly at high pressures (Fischer et al. 2013), it is important to place better constraints on the thermoelastic parameters of these alloys at high *P*-*T*. Such EoS will provide an accurate formulation to model the structure and composition of telluric planetary interiors.

Thus, we performed a systematic X-ray diffraction study of iron-silicon alloys in the B2 and hcp+B2 stability fields over a large compositional (7–30 wt% Si), pressure (20–120 GPa), and temperature (1100–3000 K) range. A composition-dependent parameterized thermal equation of state for Fe-Si alloys in the B2 structure is constructed using here-obtained experimental unit-cell volumes of single B2/DO_3 phases and available literature reports. The thermal equation of state is applied to calculate the composition and densities of B2 phases coexisting with hcp phases, which provides new constraints on the Si-rich side of the Fe-FeSi phase diagram. Finally, implications of our results concerning the buoyancy of solid Fe-Si alloys crystallizing in Mercury's core are discussed, as solid-liquid density contrast is crucial to constrain core structure and dynamics.

METHODS

Foils of iron-silicon alloys with thicknesses ranging 2–5 μm were prepared by physical vapor deposition (PVD) at the Institut de Minéralogie, de Physique des Matériaux et de Cosmochimie (IMPMC). They were confirmed to be chemically homogeneous Fe-7.1(3)wt%Si (Fe7Si), Fe-16.0(5)wt%Si (Fe16Si), Fe-22.0(5)wt%Si (Fe22Si), and Fe-30(2)wt%Si (Fe30Si) alloys by scanning electron microscopy (SEM) measurements. At ambient conditions, they are observed to be nano-grained bcc alloys (Fe7Si), amorphous (Fe16Si and Fe22Si), or a mixture of amorphous and nano-grained alloys (Fe30Si). High *P-T* conditions were generated by a laser heated, Le Toullec-type membrane-driven diamond anvil cell (LH-DAC) equipped with diamond anvils of flat 350 μm, 250 μm, or beveled 150/300 μm culets, depending on target pressures. The sample was loaded into the hole of a pre-indented rhenium gasket sandwiched between two layers of 10–20 μm thick KCl that behave as thermal insulators and pressure media. The whole DAC plus sample assembly was subsequently dried in a vacuum oven at ~393 K for several hours and then rapidly sealed in order to avoid sample oxidation or moisture absorption by the KCl.

In situ angle dispersive X-ray diffraction (XRD) measurements were performed at the beamline P02.2 at Petra III. Monochromatic X-rays with a wavelength of 0.2901 Å were focused to a spot at the sample's position of ~2 μm × 2 μm full width at half maximum. Diffraction patterns were collected using a Perkin Elmer flat panel detector. Samples were heated from both sides with a single Nd:YAG laser split into two optical paths. The heated area was ~20 μm × 20 μm, significantly larger than the X-ray beam, so as to minimize radial temperature gradients. Temperature was measured by a spectroradiometric method. Errors in temperature are ±5%.

Isothermal measurements with increasing pressure were conducted for Fe22Si with *T* kept at 1500–1600 K and *P* ranging between 40 and 100 GPa. Further quasi-isobaric measurements with increasing laser power were performed for all samples for selected pressures in the range spanning between 20 and 120 GPa. XRD patterns and temperature measurements were collected in parallel for each investigated thermodynamic point. Alignment of the X-ray beam and the laser-heated spot was confirmed before and after successive heating cycles.

Sample to detector distance and detector orientation were calibrated with a CeO_2 standard. Collected diffraction images were azimuthally integrated using the software Dioptas (Prescher and Prakapenka 2015) and analyzed with the Le Bail method using the software JANA2006 (Petříček et al. 2014) (Figure 1). Integrated diffraction patterns where sample peak positions strongly deviated from the refined Le Bail fit have been omitted from the present dataset as these typically indicate the presence of strong non-hydrostatic effects.

Pressure was determined from the volume of KCl at high temperature (Dewaele et al. 2012). Temperature of KCl was corrected from the measured temperature following Campbell et al. (2009):

$$T_{KCl} = \frac{3T_{meas}+300}{4} \tag{1}$$

Total errors in pressure were estimated as the sum of 2% of the pressure at 300 K, to account for intrinsic uncertainties in the calibration used, and 50% of thermal pressure due to uncertainties in KCl temperature and thermal parameters (Dewaele et al. 2012; Tateno et al. 2019).

VOLUME AND THERMAL EoS OF B2 Fe-Si ALLOYS

Fe22Si exhibited a single B2 phase throughout the measured experimental conditions (~20–120 GPa and 2500–3000 K), while a single B2/DO_3 phase was observed at only <42 GPa in Fe16Si, and >27 GPa in Fe30Si. Data were collected for hcp+B2 mixtures at 86–93 GPa in the case of Fe16Si starting material and at 33–99 GPa in the case of Fe7Si starting material. The DO_3 phase, observed in Fe16Si only at ~25–35 GPa, is an fcc superlattice of B2 FeSi and bcc Fe, where off-stoichiometric alloys exhibit disorder on the Si sites of the lattice (Randl et al. 1995). Volume differences between the B2 and DO_3 phases were not resolvable at the *P-T* conditions where both phases were observed. The obtained B2/DO_3 *P-V-T* datasets (Supporting Table 1) along with the ambient and high-temperature volumes of Fe-16wt%Si alloys and stoichiometric FeSi reported in previous experimental studies (Fischer et al. 2012; Fischer et al. 2014) were fitted to a model based on the Mie-Grüneisen-Debye equation of state. As constraints for room-*T* volume, we included room-*T* data of the B2 or DO_3 phase measured in alloys containing 9–17wt%Si (Fischer et al. 2012; Fischer et al. 2014; Edmund et al. 2019b) as B2 and DO_3 alloys have been reported to have similar elastic properties (Fischer et al. 2014; Karel et al. 2015; Edmund et al. 2019b). *P-V* relations at room temperature are described by the third-order Birch-Murnaghan equation of state:

$$P_{300K} = \frac{3}{2}K_0\left[\left(\frac{V_0}{V}\right)^{\frac{7}{3}} - \left(\frac{V_0}{V}\right)^{\frac{5}{3}}\right]\left[1 + \frac{3}{4}(K' - 4)\left\{\left(\frac{V_0}{V}\right)^{\frac{2}{3}} - 1\right\}\right] , \quad (2)$$

where V_0 is the volume at ambient pressure, K_0 is the bulk modulus, and K' is its pressure derivative. Thermal pressure P_{th} is expressed by the Mie-Grüneisen equation of state:

$$P_{th} = \frac{\gamma}{V}[E(T, \theta_D) - E(300\mathrm{K}, \theta_D)] , \quad (3)$$

with the Grüneisen parameter given by

$$\gamma = \gamma_0 \left(\frac{V}{V_0}\right)^q , \tag{4}$$

where γ_0 is the ambient pressure Grüneisen parameter and q accounts for its volume dependence. The quasi-harmonic internal energy $E(T, \theta_D)$ is calculated according to the Debye model:

$$E(T, \theta_D) = 9nRT \left(\frac{T}{\theta_D}\right)^3 \int_0^{\frac{\theta_D}{T}} \frac{x^3}{e^x - 1} dx , \tag{5}$$

where n is the number of atoms and R is the gas constant. The Debye temperature θ_D is calculated by

$$\theta_D = \theta_0 \exp\left(\frac{\gamma_0 - \gamma}{q}\right) , \tag{6}$$

where θ_0 is the Debye temperature at V_0. The value of θ_0 is set to that of iron (Dewaele et al. 2006) as commonly done for B2 Fe-Si alloys (Fischer et al. 2012; Fischer et al. 2014).

To account for the composition dependence observed in the experimental data, we assumed a second-order dependence on X_{Si} (mole fraction of silicon) for K_0 and a linear dependence on X_{Si} for V_0, K', and γ_0. EoS parameters of FeSi (X_{Si}=0.5) at room-T were fixed to the values obtained from a combined fit to available literature data (Sata et al. 2010; Ono 2013; Fischer et al. 2014), with rescaled pressures consistent with the pressure scale employed in the present study (Dewaele et al. 2012). Also, X_{Si} dependence of V_0 was fixed to the result of a linear fit to previous studies described in Edmund et al. (2019b). Fitting results are shown in Table 1 and Supporting Table 2 and compared to experimental observations in Figure 2.

We observe that the volume of the alloys decreases with Si content over the measured P-T-X_{Si} conditions. Likely related to this, the bulk modulus increases with Si content in the 20–50 at% Si range (~11–33.5 wt%). A K_0 value of ~165–170 GPa at 20–30 at% Si is consistent with the adiabatic bulk modulus of single crystals of Fe-Si alloys obtained by ultrasonic methods (Machová & Kadečková 1977). Some earlier experimental studies at room-T argued that Fe-Si alloys in B2/DO_3 structure, namely Fe-17.0wt%Si and 17.8wt%Si, are less compressible than what is reported here (Lin et al. 2003; Hirao et al. 2004). This discrepancy is likely caused by non-hydrostatic compression of the sample in those experiments. Indeed, no pressure medium was used in Hirao et al. (2004), and an ethanol:methanol:water mixture was employed as pressure-transmitting medium in Lin et al. (2003), which becomes strongly non-hydrostatic at pressures above 12 GPa (Klotz et al. 2009). In the present study, stress is effectively released by laser heating, ensuring quasi-hydrostatic conditions.

Thermal EoS obtained in the present study indicates that thermal expansion is larger in alloys with low Si content. Although our thermal EoS was obtained from high-pressure data, the fitting result well reproduces the thermal expansion measured at ambient pressure on alloys with ~25 at% Si (Farquhar 1945; Lihl & Ebel 1961).

Fe-FeSi PHASE DIAGRAM

Coexistence of B2 and hcp phases was observed at 33–99 GPa in measurements on Fe7Si starting material, and 86–93 GPa in measurements on Fe16Si starting material (Supporting Table 3). The DO_3 phase was never found in coexistence with the hcp structure over the experimental conditions of this study. Kuwayama et al. (2009) and Fischer et al. (2013) reported a single hcp phase stable at low temperature for starting materials with ~10 wt% Si (<~1700 K at 50 GPa) and ~9 wt% Si (<~1300 K at 50 GPa), respectively. However, here we never observed a single hcp phase, not even for the Fe7Si alloy at low temperature (1100–1300 K). The wide hcp stability field at low temperature reported in previous studies is likely a consequence of the slow kinetics of phase transformation from hcp to hcp+B2 (Nakajima et al. 2020). As the PVD samples used in the present study were synthesized into out-of-equilibrium states, they rapidly equilibrate upon heating to the most thermodynamically favorable assemblage at the investigated *P*-*T* conditions, effectively overcoming kinetic barriers. Grain growth of the B2 phase was observed right away upon heating, even at the lowest measured temperature (Supporting Figure 1). In contrast, cold compression does not necessarily promote thermodynamic stabilization, and XRD patterns here collected on starting materials at room *T* and high *P* highlight structures different from phase stability expected according to previous room temperature studies (Lin et al. 2003; Hirao et al. 2004; Kuwayama et al. 2009) with the bcc structure here observed till higher pressures and a larger domain of coexistence of bcc and hcp phases (Supporting Figure 2).

Compositions of coexisting hcp and B2 phases provide boundaries for the hcp+B2 coexistence region. While, in the hcp phase, Si alloying does not strongly influence the volume (e.g. Morrison et al. 2018; Kamada et al. 2018; Edmund 2019a; Edmund et al. 2020), B2/DO_3 volumes vary significantly with composition (Edmund et al. 2019b). Provided that the volume of the B2 phase and experimental conditions (*P* and *T*) are known, Si content can be estimated using the parameterized P-V-T-X_{Si} equation of state previously presented. The so-calculated compositions of the B2 phase in coexistence with the hcp phase are shown in Figure 3a. They range from 13wt% Si at ~30 GPa to 18 wt% Si at ~100 GPa. Observation of a single B2 phase in Fe22Si throughout the measured *P*-*T* range is well reproduced within the calculated boundary. The present experiments and a previous study (Fischer et al. 2012) observed a single B2/DO_3 phase in Fe16Si at pressures below ~40 GPa and 60–80 GPa, respectively. These observations are also consistent with the calculated phase boundary (~15–16 wt% Si at 80 GPa).

Over the pressure range of interest of the present study, the temperature dependence of the slope of the hcp+B2/B2 boundary was below the detection limit of the applied method (Figure 3a), compatible with a value of ~2 wt% Si per 1000 K as proposed in a previous study (Fischer et al. 2013). On the basis of our data, positive temperature dependence in Si content below 42 GPa cannot be excluded, but this becomes negligible at higher pressure.

The hcp+B2/B2 boundary moves towards the Si-rich side with increasing pressure, consistent with previous studies (Kuwayama et al. 2009; Fischer et al. 2013) (Figure 3b). Kuwayama et al. (2009) reported Si concentrations of coexisting hcp and B2 phases at 45 GPa, estimated by electron microprobe analysis on recovered samples, which are about 2 wt% smaller than the present study. This difference may be attributed to underestimation of the compositional gap between coexisting phases in the electron microprobe measurements arising from the small grain sizes. The hcp/hcp+B2 boundary located in the Si-poor side of the phase diagram and estimated at 7–10 wt% Si at 50 GPa also moves toward the Si-rich side with increasing pressure at constant temperature (Kuwayama et al. 2009; Fischer et al. 2013). The expansion of the hcp+B2 coexistence region towards the Si-rich side could be used as an argument in favor of an increase of eutectic Si content in an Fe-FeSi system with increasing pressure. This supports a small change in the eutectic Si content with increasing pressure as recently reported (Hasegawa et al. 2021) rather than a steep decrease of eutectic Si content argued on the basis of earlier determinations (Ozawa et al. 2016).

IMPLICATIONS

Silicon is thought to be a dominant light element in Mercury's core along with sulfur (e.g. Malavergne et al. 2010; Malavergne et al. 2014; Chabot et al. 2014). Estimations of bulk core Si abundances can reach 25 wt% (Chabot et al. 2014). Knowledge of the Fe-FeSi phase diagram and of the thermo-elastic properties of stable phases at relevant *P*-*T* conditions is thus essential to accurately determine the structure and dynamics of Mercury's core, and in particular to model dynamo mechanisms within the core capable of explaining Mercury's exotic magnetic field (e.g. Anderson et al. 2011; Johnson et al. 2016). Compositional convection driven by core solidification is one of the main power sources for a long-standing dynamo (Stevenson 2003), and the density contrast between the crystallizing material and the coexisting liquid controls whether the solid sinks down to form an inner core, or rises up to form a layer at the core-mantle boundary. Clearly, these two scenarios lead to profoundly different core structures and dynamics.

Si-rich core compositions exceeding the Fe-FeSi eutectic (~10–15 wt% at ~50 GPa according to Hasegawa et al. 2021) would crystallize a B2 solid, which is more enriched in Si than the liquid. Whether the solid B2 Fe-Si alloy sinks or floats depends on whether the effect of increased Si content on density is sufficient to overcome the density difference due to solidification. Figure 4a illustrates the density of solid B2 Fe-Si alloys calculated using the parameters of the present study and liquid Fe-Si alloys based on Terasaki et al. (2019) over the 30–40 GPa pressure range, corresponding to the central pressure of Mercury's Fe-Si core (Knibbe & van Westrenen 2015). Densities have been evaluated at the melting temperature of Fe16Si (Asanuma et al. 2010; Morard et al. 2011; Fischer et al. 2012). It is observed that liquid and solid densities are similar for Si concentrations approaching 10 wt%, while a solid is significantly denser for stoichiometric FeSi. In the case of Fe16Si alloy, which has been investigated by both the present study and Terasaki et al. (2019), the solid-liquid density contrast is equivalent to a difference of ~7–8 wt% in Si content.

Figure 4b illustrates the density contrast between solid and liquid Fe-Si alloys for Si concentrations 10–33.5 wt%, under the assumption of a narrow melting loop, corresponding to Si solid-liquid partitioning close to 1. Differences in Si content of solid and coexisting liquid are estimated at ~1 wt% at 2 GPa (Morard et al. 2014) and below 2 wt% at 50 GPa (Fischer et al. 2013; Ozawa et al. 2016), supporting the overall validity of this first-order approximation. The solid-liquid density contrast increases with increasing

Si content of the bulk core. Crystallizing B2 alloys (with possible exception of those with Si content approaching 10 wt%) are suggested to be sufficiently dense to gravitationally segregate to form a solid inner core. On the other hand, a liquid with 22 wt% Si or more, although unlikely for Mercury (c.f. Genova et al. 2019; Terasaki et al. 2019), is light enough to have a B2 inner core regardless of the solid composition (Figure 4).

Ultimately, given the large stability field of the B2 phase in Fe-Si alloys, this structure is a primary candidate for solid inner cores of Si-rich telluric planets having formed under reducing conditions. Future determinations of the eutectic point and the melting loop of Fe-Si alloys over an extended *P*-*T* range are however required to confirm the possibility of a B2 inner core in Mercury.

ACKNOWLEDGMENTS

Authors wish to thank A. Boury for PVD sample synthesis, R. Husband and N. Giordano for temperature calibration testing on Petra III beamline P02.2. We also thank A. Rivoldini for fruitful discussions. This project has received funding from the European Research Council (ERC) under the European Union's Horizon 2020 Research and Innovation Programme (grant agreement No. 724690). PVD machines at IMPMC have been supported by the European Research Council (ERC) under the European Union

Horizon 2020 Research and Innovation Programme (grant agreement No.670787). M.A.B. has received funding from ERC under the European Union's Horizon 2020 Research and Innovation Programme (grant agreement No. 670787). The Scanning Electron Microscope facilities at IMPMC are supported by Région 415 Ile-de-France grant SESAME 2006 No. I-07-593/R, INSU-CNRS, Institut 416 de Physique (INP)-CNRS, Université Pierre et Marie Curie-Paris 6, and by 417 the French National Research Agency (ANR) grant ANR-07-BLAN-0124-01. We acknowledge DESY (Hamburg, Germany), a member of the Helmholtz Association HGF, for the provision of experimental facilities. This research was carried out at P02.2 beamline of Petra III. Comments from two anonymous reviewers were helpful to improve the manuscript.

REFERENCES CITED

Anderson, B.J., Johnson, C.L., Korth, H., Purucker, M.E., Winslow, R.M., Slavin, J.A., Solomon, S.C., McNutt Jr., R.L., Raines, J.M., and Zurbuchen, T.H. (2011) The global magnetic field of Mercury from MESSENGER orbital observations. Science, 333(6051), 1859-1862.

Antonangeli, D., Morard, G., Paolasini, L., Garbarino, G., Murphy, C.A., Edmund, E., Decremps, F., Fiquet, G., Bosak, A., Mezouar, M., and Fei, Y. (2018) Sound velocities and density measurements of solid hcp-Fe and hcp-Fe–Si (9 wt.%) alloy at high pressure: Constraints on the Si abundance in the Earth's inner core. Earth and Planetary Science Letters, 482, 446-453.

Asanuma, H., Ohtani, E., Sakai, T., Terasaki, H., Kamada, S., Kondo, T., and Kikegawa, T. (2010) Melting of iron–silicon alloy up to the core–mantle boundary pressure: implications to the thermal structure of the Earth’s core. Physics and Chemistry of Minerals, 37(6), 353-359.

Badro, J., Brodholt, J.P., Piet, H., Siebert, J., and Ryerson, F.J. (2015) Core formation and core composition from coupled geochemical and geophysical constraints. Proceedings of the National Academy of Sciences, 112(40), 12310-12314.

Brosh, E., Makov, G., and Shneck, R.Z. (2009). Thermodynamic analysis of high-pressure phase equilibria in Fe–Si alloys, implications for the inner-core. Physics of the Earth and Planetary Interiors, 172(3-4), 289-298.

Campbell, A.J., Danielson, L., Righter, K., Seagle, C.T., Wang, Y., and Prakapenka, V.B. (2009) High pressure effects on the iron–iron oxide and nickel–nickel oxide oxygen fugacity buffers. Earth and Planetary Science Letters, 286(3-4), 556-564.

Chabot, N.L., Wollack, E.A., Klima, R.L., and Minitti, M.E. (2014) Experimental constraints on Mercury's core composition. Earth and Planetary Science Letters, 390, 199-208.

Cui, S., and Jung, I.H. (2017) Critical reassessment of the Fe-Si system. Calphad, 56, 108-125.

Dewaele, A., Loubeyre, P., Occelli, F., Mezouar, M., Dorogokupets, P. I., and Torrent, M. (2006). Quasihydrostatic equation of state of iron above 2 Mbar. Physical Review Letters, 97(21), 215504.

Dewaele, A., Belonoshko, A.B., Garbarino, G., Occelli, F., Bouvier, P., Hanfland, M., and Mezouar, M. (2012) High-pressure–high-temperature equation of state of KCl and KBr. Physical Review B, 85(21), 214105.

Edmund, E., Antonangeli, D., Decremps, F., Miozzi, F., Morard, G., Boulard, E., Clark, A.N., Ayrinhac, S., Gauthier, M., Morand, M., and Mezouar, M. (2019a) Velocity-Density Systematics of Fe-5wt% Si: Constraints on Si Content in the Earth's Inner Core. Journal of Geophysical Research: Solid Earth, 124(4), 3436-3447.

Edmund, E., Antonangeli, D., Decremps, F., Morard, G., Ayrinhac, S., Gauthier, M., Boulard, E., Mezouar, M., Hanfland, M., and Guignot, N. (2019b) Structure and elasticity of cubic Fe-Si alloys at high pressures. Physical Review B, 100(13), 134105.

Edmund, E., Miozzi, F., Morard, G., Boulard, E., Clark, A., Decremps, F., Garbarino, G., Svitlyk, V., Mezouar, M., and Antonangeli, D. (2020) Axial Compressibility and

Thermal Equation of State of Hcp Fe–5wt% Ni–5wt% Si. Minerals, 10(2), 98.

Farquhar, M. C. M., Lipson, H., and Weill, A. R. (1945). An X-ray study of iron-rich iron-silicon alloys. Journal of the Iron and Steel Institute, 152(2), 457.

Fei, Y., Murphy, C., Shibazaki, Y., Shahar, A., and Huang, H. (2016) Thermal equation of state of hcp-iron: Constraint on the density deficit of Earth's solid inner core. Geophysical Research Letters, 43(13), 6837-6843.

Fischer, R.A., Campbell, A.J., Caracas, R., Reaman, D.M., Dera, P., and Prakapenka, V.B. (2012) Equation of state and phase diagram of Fe–16Si alloy as a candidate component of Earth's core. Earth and Planetary Science Letters, 357, 268-276.

Fischer, R.A., Campbell, A.J., Reaman, D.M., Miller, N.A., Heinz, D.L., Dera, P., and Prakapenka, V.B. (2013) Phase relations in the Fe–FeSi system at high pressures and temperatures. Earth and Planetary Science Letters, 373, 54-64.

Fischer, R.A., Campbell, A.J., Caracas, R., Reaman, D.M., Heinz, D.L., Dera, P., and Prakapenka, V.B. (2014) Equations of state in the Fe-FeSi system at high pressures and temperatures. Journal of Geophysical Research: Solid Earth, 119(4), 2810-2827.

Geballe, Z.M., and Jeanloz, R. (2014) Solid phases of FeSi to 47 GPa and 2800 K: New data. American Mineralogist, 99(4), 720-723.

Genova, A., Goossens, S., Mazarico, E., Lemoine, F.G., Neumann, G.A., Kuang, W., Sabaka, T.J., Hauck, S.A., Smith, D.E., Solomon, S.C., and Zuber, M.T. (2019) Geodetic evidence that Mercury has a solid inner core. Geophysical Research Letters, 46(7), 3625-3633.

Hasegawa, M., Hirose, K., Oka, K., and Ohishi, Y. (2021). Liquidus phase relations and solid-liquid partitioning in the Fe-Si-C system under core pressures. Geophysical Research Letters, 48(13), e2021GL092681.

Hirao, N., Ohtani, E., Kondo, T., and Kikegawa, T. (2004) Equation of state of iron–silicon alloys to megabar pressure. Physics and chemistry of minerals, 31(6), 329-336.

Johnson, C.L., Philpott, L.C., Anderson, B.J., Korth, H., Hauck, S.A., Heyner, D., Phillips, R.J., Einslow, R.M., and Solomon, S.C. (2016) MESSENGER observations of induced magnetic fields in Mercury's core. Geophysical Research Letters, 43(6), 2436-2444.

Kamada, S., Suzuki, N., Maeda, F., Hirao, N., Hamada, M., Ohtani, E., Masuda, R., Mitsui, T., Ohishi, Y., and Nakano, S. (2018) Electronic properties and compressional behavior of Fe–Si alloys at high pressure. American Mineralogist: Journal of Earth and Planetary Materials, 103(12), 1959-1965.

Karel, J., Juraszek, J., Minar, J., Bordel, C., Stone, K.H., Zhang, Y.N., Hu, J., Wu, R.Q., Ebert, H., Kortright, J.B., and Hellman, F. (2015) Effect of chemical order on the magnetic and electronic properties of epitaxial off-stoichiometry F e x S i 1− x thin films. Physical Review B, 91(14), 144402.

Kilburn, M.R., and Wood, B.J. (1997) Metal–silicate partitioning and the incompatibility of S and Si during core formation. Earth and Planetary Science Letters, 152(1-4), 139-148.

Klotz, S., Chervin, J.C., Munsch, P., and Le Marchand, G. (2009) Hydrostatic limits of 11 pressure transmitting media. Journal of Physics D: Applied Physics, 42(7), 075413.

Knibbe, J.S., and van Westrenen, W. (2015) The interior configuration of planet Mercury constrained by moment of inertia and planetary contraction. Journal of Geophysical Research: Planets, 120(11), 1904-1923.

Knibbe, J.S., and van Westrenen, W. (2018) The thermal evolution of Mercury's Fe–Si core. Earth and Planetary Science Letters, 482, 147-159.

Komabayashi, T., Fei, Y., Meng, Y., and Prakapenka, V. (2009) In-situ X-ray diffraction measurements of the γ-ε transition boundary of iron in an internally-heated diamond anvil cell. Earth and Planetary Science Letters, 282(1-4), 252-257.

Komabayashi, T., Pesce, G., Morard, G., Antonangeli. D., Sinmyo, R., and Mezouar, M. (2019) Phase transition boundary between fcc and hcp structures in Fe-Si alloy and its implications for terrestrial planetary cores. American Mineralogist, 104, 94–99.

2019.

Kuwayama, Y., Sawai, T., Hirose, K., Sata, N., and Ohishi, Y. (2009) Phase relations of iron–silicon alloys at high pressure and high temperature. Physics and Chemistry of Minerals, 36(9), 511-518.

Lihl, F., and Ebel, H. (1961). X-ray examination of the structure of iron-rich alloys of the iron-silicon system. Arch. Eisenhuettenwes, 32, 489-491.

Lin, J.F., Campbell, A.J., Heinz, D.L., and Shen, G. (2003) Static compression of iron-silicon alloys: Implications for silicon in the Earth's core. Journal of Geophysical Research: Solid Earth, 108(B1).

Lin, J.F., Scott, H.P., Fischer, R.A., Chang, Y.Y., Kantor, I., and Prakapenka, V.B. (2009) Phase relations of Fe-Si alloy in Earth's core. Geophysical Research Letters, 36(6).

Machová, A., and Kadečková, S. (1977) Elastic constants of iron-silicon alloy single crystals. Czechoslovak Journal of Physics B, 27(5), 555-563.

Malavergne, V., Toplis, M.J., Berthet, S., and Jones, J. (2010) Highly reducing conditions during core formation on Mercury: Implications for internal structure and the origin of a magnetic field. Icarus, 206(1), 199-209.

Malavergne, V., Cordier, P., Righter, K., Brunet, F., Zanda, B., Addad, A., Smith, T., Bureau, H., Surblé, S., Raepsaet, C., and others. (2014) How Mercury can be the most reduced terrestrial planet and still store iron in its mantle. Earth and Planetary Science Letters, 394, 186-197.

McGuire, C., Santamaria-Pérez, D., Makhluf, A., and Kavner, A. (2017) Isothermal equation of state and phase stability of Fe5Si3 up to 96 GPa and 3000 K. Journal of Geophysical Research: Solid Earth, 122(6), 4328-4335.

Morard, G., Andrault, D., Guignot, N., Siebert, J., Garbarino, G., and Antonangeli, D. (2011) Melting of Fe–Ni–Si and Fe–Ni–S alloys at megabar pressures: implications for the core–mantle boundary temperature. Physics and Chemistry of Minerals, 38(10), 767-776.

Morard, G., Siebert, J., & Badro, J. (2014) Partitioning of Si and platinum group elements between liquid and solid Fe–Si alloys. Geochimica et Cosmochimica Acta, 132, 94-100.

Morrison, R.A., Jackson, J.M., Sturhahn, W., Zhang, D., and Greenberg, E. (2018) Equations of State and Anisotropy of Fe-Ni-Si Alloys. Journal of Geophysical Research: Solid Earth, 123(6), 4647-4675.

Nakajima, Y., Kawaguchi, S.I., Hirose, K., Tateno, S., Kuwayama, Y., Sinmyo, R., Ozawa, H., Tsutsui, S., Uchiyama, H., and Baron, A.Q. (2020) Silicon-Depleted Present-Day Earth's Outer Core Revealed by Sound Velocity Measurements of Liquid Fe-Si

Alloy. Journal of Geophysical Research: Solid Earth, 125(6), e2020JB019399.

Nittler, L.R., Starr, R.D., Weider, S.Z., McCoy, T.J., Boynton, W.V., Ebel, D.S., Ernst, C.M., Evans, L.G., Goldsten, J.O., Hamara, D.K., and others. (2011) The major-element composition of Mercury's surface from MESSENGER X-ray spectrometry. Science, 333(6051), 1847-1850.

Ono, S. (2013) Equation of state and elasticity of B2-type FeSi: Implications for silicon in the inner core. Physics of the Earth and Planetary Interiors, 224, 32-37.

Ozawa, H., Hirose, K., Yonemitsu, K., and Ohishi, Y. (2016) High-pressure melting experiments on Fe–Si alloys and implications for silicon as a light element in the core. Earth and Planetary Science Letters, 456, 47-54.

Petříček, V., Dušek, M., and Palatinus, L. (2014) Crystallographic computing system JANA2006: general features. Zeitschrift für Kristallographie-Crystalline Materials, 229(5), 345-352.

Ponomareva, A.V., Ruban, A.V., Dubrovinskaia, N., Dubrovinsky, L., and Abrikosov, I.A. (2009) Influence of global magnetic state on chemical interactions in high-pressure high-temperature synthesis of B 2 Fe 2 Si. Applied Physics Letters, 94(18), 181912.

Prescher, C., and Prakapenka, V.B. (2015) DIOPTAS: a program for reduction of two-dimensional X-ray diffraction data and data exploration. High Pressure

Research, 35(3), 223-230.

Randl, O.G., Vogl, G., Petry, W., Hennion, B., Sepiol, B., and Nembach, K. (1995) Lattice dynamics and related diffusion properties of intermetallics: I. Fe3Si. Journal of Physics: Condensed Matter, 7(30), 5983.

Ricolleau, A., Fei, Y., Corgne, A., Siebert, J., and Badro, J. (2011) Oxygen and silicon contents of Earth's core from high pressure metal–silicate partitioning experiments. Earth and Planetary Science Letters, 310(3-4), 409-421.

Sata, N., Hirose, K., Shen, G., Nakajima, Y., Ohishi, Y., and Hirao, N. (2010) Compression of FeSi, Fe3C, Fe0. 95O, and FeS under the core pressures and implication for light element in the Earth's core. Journal of Geophysical Research: Solid Earth, 115(B9).

Stevenson, D.J. (2003) Planetary magnetic fields. Earth and Planetary Science Letters, 208(1-2), 1-11.

Tateno, S., Kuwayama, Y., Hirose, K., and Ohishi, Y. (2015) The structure of Fe–Si alloy in Earth's inner core. Earth and Planetary Science Letters, 418, 11-19.

Tateno, S., Komabayashi, T., Hirose, K., Hirao, N., and Ohishi, Y. (2019). Static compression of B2 KCl to 230 GPa and its P-V-T equation of state. American Mineralogist, 104(5), 718-723.

Terasaki, H., Rivoldini, A., Shimoyama, Y., Nishida, K., Urakawa, S., Maki, M., Kurokawa, F., Takubo, Y., Shibazaki, Y., Sakamaki, T., and others. (2019) Pressure and composition effects on sound velocity and density of core-forming liquids: Implication to core compositions of terrestrial planets. Journal of Geophysical Research: Planets, 124(8), 2272-2293.

TABLE 1. Parameters for the thermal equation of state established in the present study in comparison to those of Fe-Si alloys.

	This study	B2 FeSi[a]	DO3 Fe-16Si[b]	hcp Fe-9Si[a]
V_0 (cm^3/mol)	6.419-1.536(X_{Si}-0.5) (fixed)	6.414	6.799	7.203
K_0 (GPa)	223+(382±13)(X_{Si}-0.5) +(616±41)(X_{Si}-0.5)^2	230.6	193.4	129.1
K'	4.3-(4.9±0.6)(X_{Si}-0.5)	4.17	4.91	5.29
θ_0 (K)	417 (fixed)	417	417	417
γ_0	1.93±0.13-(2.59±0.45)(X_{Si}-0.5)	1.3	1.89	1.14
q	1.8±0.4	1.7	1	1

a: Fischer et al. (2014)

b: Fischer et al. (2012)

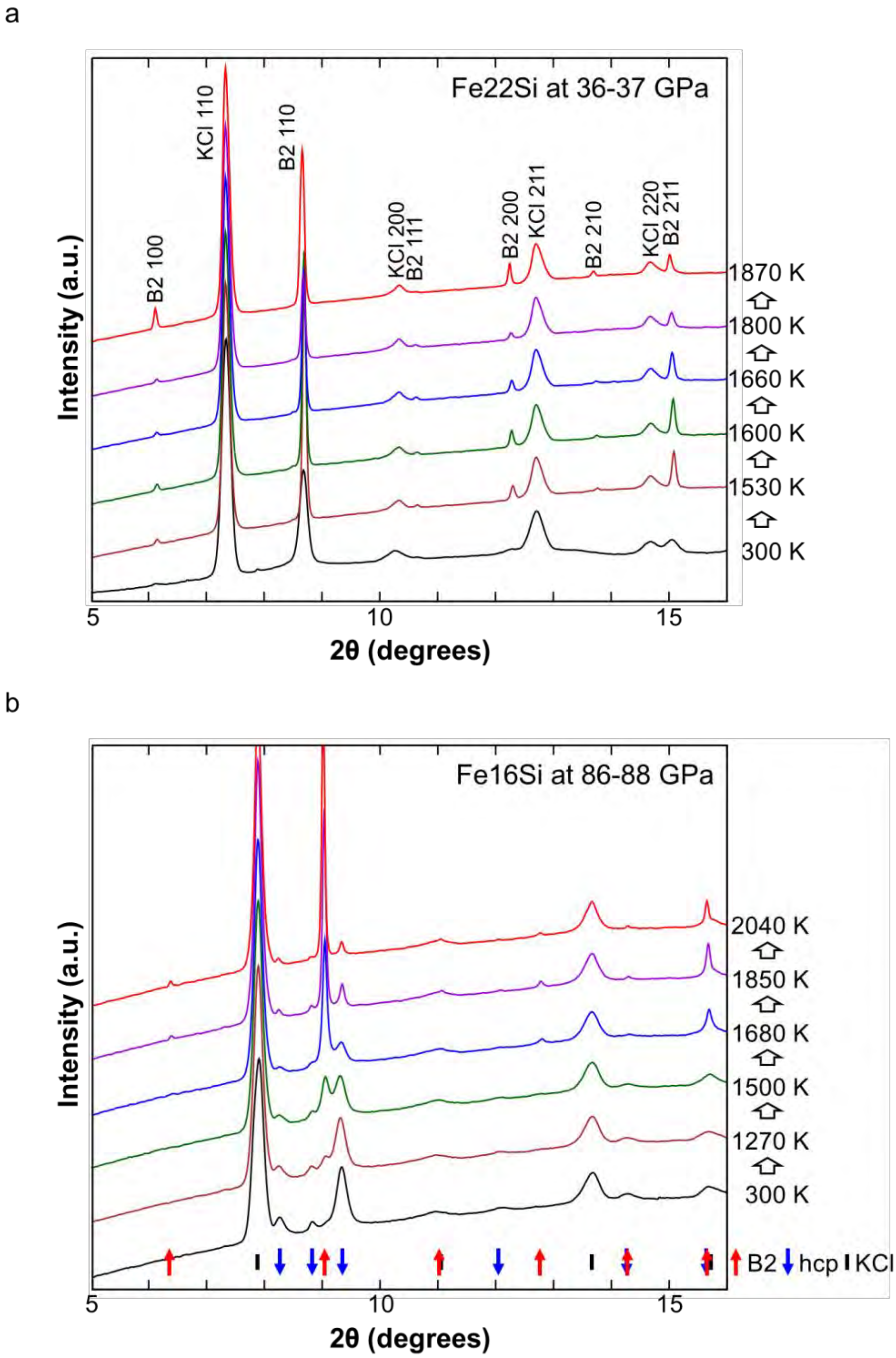

FIGURE 1. (**a**) X-ray diffraction patterns of Fe22Si at 36–37 GPa and 300–1870 K. Fe22Si remained in the B2 phase over the *P*-*T* range studied. (**b**) X-ray diffraction patterns of Fe16Si at 86-88 GPa and 300–2040 K. Red and blue arrows indicate the peak positions

of B2 and hcp phases, respectively. While the intensity of the KCl peaks remains nearly constant, significant changes in the B2 and hcp phase fractions occur at the lowest temperatures studied, above which the ratio of the two phases no longer changes. To minimize possible effects arising from kinetic barriers at low temperatures, only data obtained at sufficiently high temperatures to recrystallize the sample and relax non-hydrostatic stresses were used in the study.

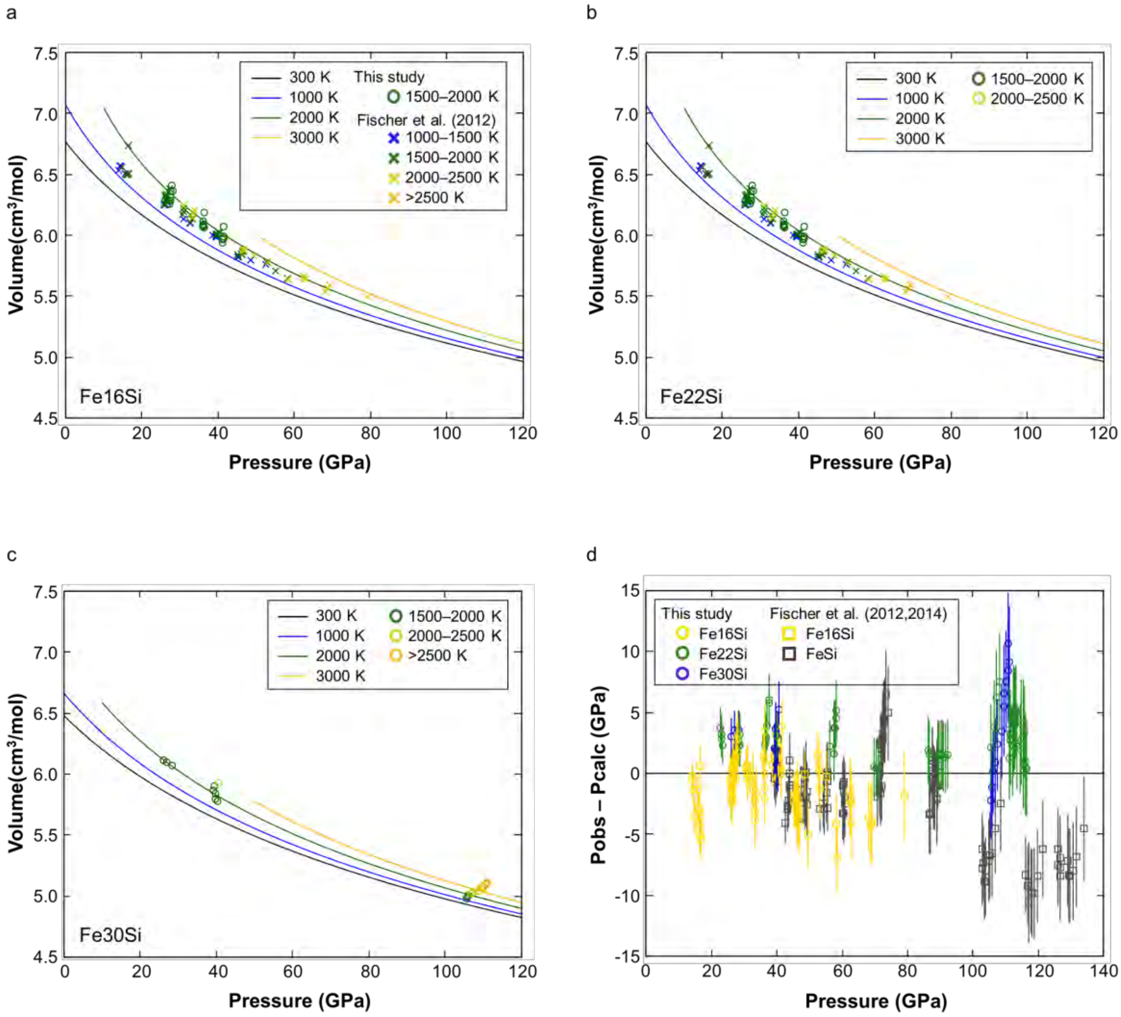

FIGURE 2. Compression curves of Fe16Si (**a**), Fe22Si (**b**), and Fe30Si (**c**) in the B2 structure at 300 K (black line), 1000 K (blue line), 2000 K (green line), and 3000 K (orange line) calculated according to the thermal equation of state established in the present study. Measured volumes are plotted as circles (green for 1500–2000 K, yellow for 2000–2500 K, and orange for >2500 K). Volumes of Fe16Si from Fischer et al. (2012) are also plotted as crosses in **a**. (**d**) Difference in pressure between the P-V-T-X_{Si} thermal equation of state from the present study, and P-V-T datapoints at high-T of the present

study and literature. Circles (yellow for Fe16Si, green for Fe22Si, and blue for Fe30Si) are results obtained in the present study, while squares (yellow for Fe16Si and black for FeSi) are from previous studies (Fischer et al. 2012, 2014).

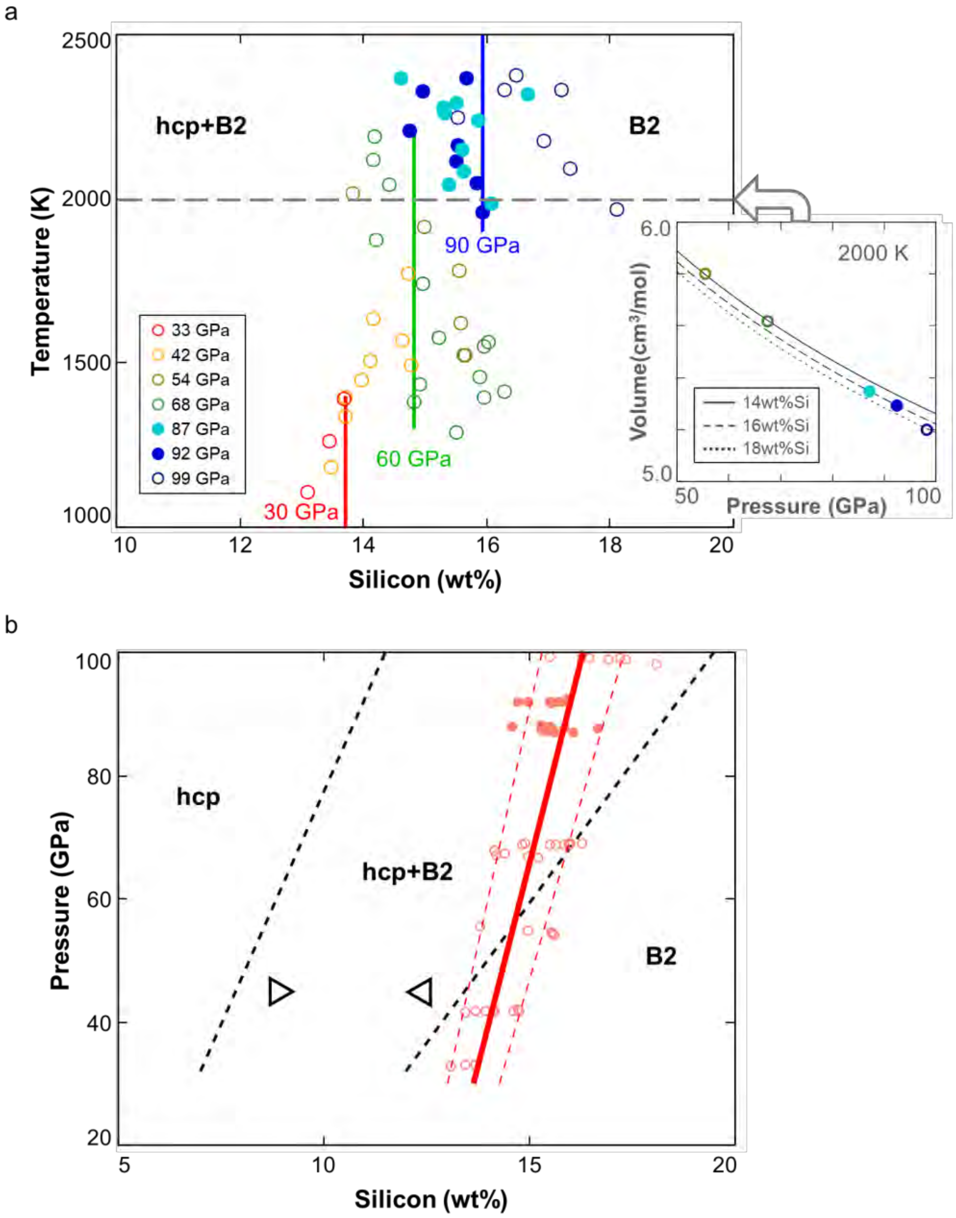

FIGURE 3. (**a**) Calculated Si content of B2 Fe-Si alloys within the hcp+B2 mixed phase region at 33–99 GPa. Open and filled circles indicate runs from Fe7Si and Fe16Si starting materials, respectively. Uncertainties in Si content are on the order of 1–1.5 wt%. Colored vertical bars indicate the hcp+B2/B2 phase boundary at 30, 60 and 90 GPa under the assumption of linear dependence on pressure, and negligible dependence on temperature.

The inset panel compares the compression curves of alloys with 14–18 wt% Si and the evolution of measured B2 volume with increasing pressure at ~2000 K. (**b**) Composition-pressure phase diagram from the present study and previous literature. The solid red line indicates the hcp+B2/B2 boundary from the present study, with uncertainties indicated by the red dashed lines. Datapoints from the present study are presented as red circles. Black dashed lines represent hcp/hcp+B2 and hcp+B2/B2 boundaries at 1500 K from Fischer et al. (2013). Triangles show the silicon contents of coexisting hcp and B2 phases at 45 GPa and 1650 K from Kuwayama et al. (2009).

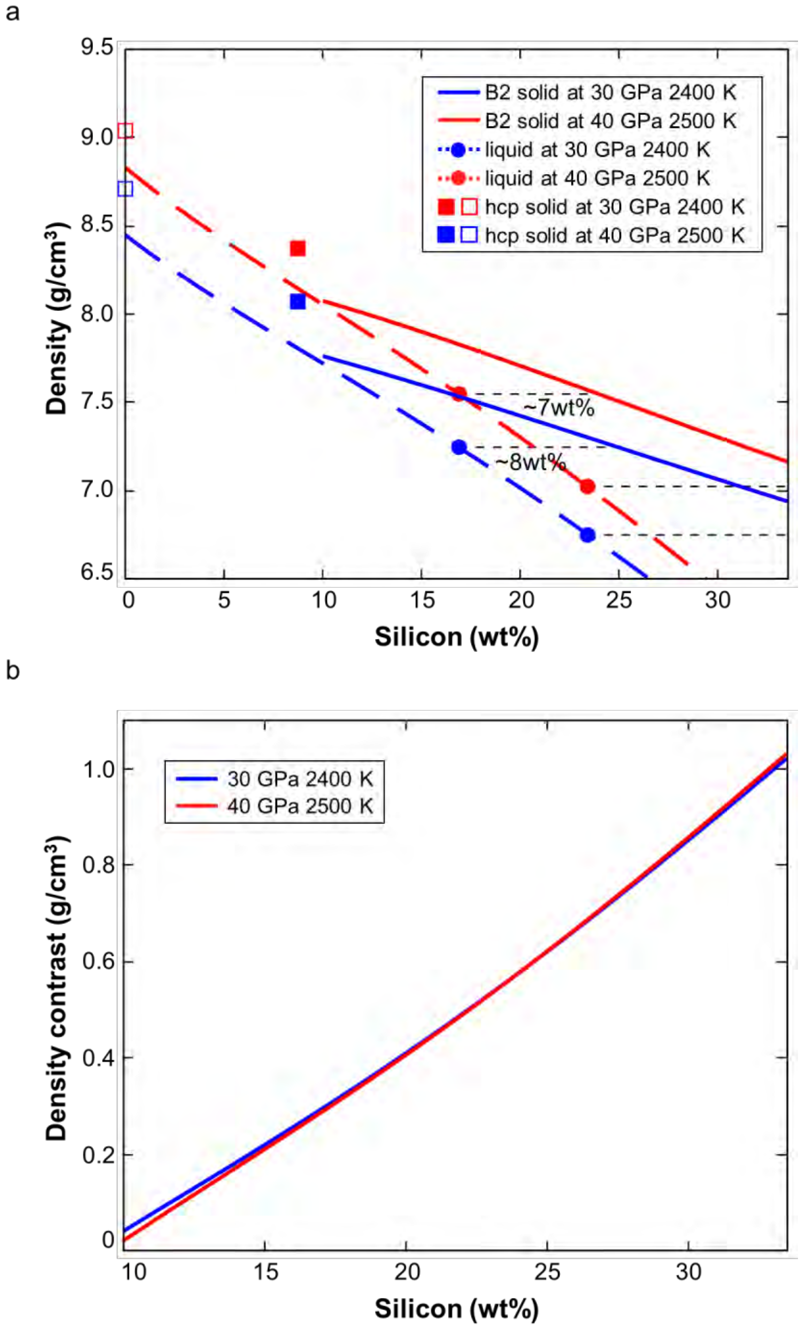

FIGURE 4. (**a**) Density of B2-structured solid and liquid Fe-Si alloys at 30 GPa and 2400 K (blue) and at 40 GPa and 2500 K (red). Solid lines indicate the densities of solid B2 alloys calculated in the present study, and dashed lines indicate liquid densities from Terasaki et al. (2019). Circles on the dashed lines indicate the sample compositions

studied in Terasaki et al. (2019). Densities of hcp-structured solid Fe and Fe-9Si are shown as open and filled squares, respectively (Fei et al. 2016; Fischer et al. 2014). (**b**) Density contrast between solid and liquid alloys at 30 GPa and 2400 K (blue), and at 40 GPa and 2500 K (red) assuming Si solid-liquid partitioning of 1.

	This study	B2 FeSi[a]	DO3 Fe-16Si[b]	hcp Fe-9Si[a]
V_0 (cm^3/mol)	6.419-1.536(X_{Si}-0.5) (fixed)	6.414	6.799	7.203
K_0 (GPa)	223+(382±13)(X_{Si}-0.5) +(616±41)(X_{Si}-0.5)^2	230.6	193.4	129.1
K'	4.3-(4.9±0.6)(X_{Si}-0.5)	4.17	4.91	5.29
θ_0 (K)	417 (fixed)	417	417	417
γ_0	1.93±0.13-(2.59±0.45)(X_{Si}-0.5)	1.3	1.89	1.14
q	1.8±0.4	1.7	1	1